UC Davis
UC Davis Previously Published Works

Title

The time-scales probed by star formation rate indicators for realistic, bursty star formation histories from the FIRE simulations

Permalink

https://escholarship.org/uc/item/21z550ns

Journal

Monthly Notices of the Royal Astronomical Society, 501(4)

ISSN

0035-8711

Authors

Velázquez, José A Flores
Gurvich, Alexander B
Faucher-Giguère, Claude-André
et al.

Publication Date

2021-01-19

DOI

10.1093/mnras/staa3893

Peer reviewed

The time-scales probed by star formation rate indicators for realistic, bursty star formation histories from the FIRE simulations

José A. Flores Velázquez[1,2], Alexander B. Gurvich[2][⋆], Claude-André Faucher-Giguère[2], James S. Bullock[1], Tjitske K. Starkenburg[2], Jorge Moreno[3], Alexandres Lazar[1], Francisco J. Mercado[1], Jonathan Stern[2], Martin Sparre[4,5], Christopher C. Hayward[6], Andrew Wetzel[7], Kareem El-Badry[8]

[1]*Department of Physics and Astronomy, University of California, Irvine, CA 92697, USA*
[2]*Department of Physics & Astronomy and CIERA, Northwestern University, 1800 Sherman Ave, Evanston, IL 60201, USA*
[3]*Department of Physics and Astronomy, Pomona College, Claremont, CA 91711, USA*
[4]*Institut für Physik und Astronomie, Universität Potsdam, Karl-Liebknecht-Str. 24/25, 14476 Golm, Germany*
[5]*Leibniz-Institut für Astrophysik Potsdam (AIP), An der Sternwarte 16, 14482 Potsdam, Germany*
[6]*Center for Computational Astrophysics, Flatiron Institute, 162 Fifth Avenue, New York, NY 10010, USA*
[7]*Department of Physics & Astronomy, University of California, Davis, CA 95616, USA*
[8]*Department of Astronomy and Theoretical Astrophysics Center, University of California Berkeley, Berkeley, CA 94720, USA*

ABSTRACT

Understanding the rate at which stars form is central to studies of galaxy formation. Observationally, the star formation rates (SFRs) of galaxies are measured using the luminosity in different frequency bands, often under the assumption of a time-steady SFR in the recent past. We use star formation histories (SFHs) extracted from cosmological simulations of star-forming galaxies from the FIRE project to analyze the time-scales to which the Hα and far-ultraviolet (FUV) continuum SFR indicators are sensitive. In these simulations, the SFRs are highly time variable for all galaxies at high redshift, and continue to be bursty to $z = 0$ in dwarf galaxies. When FIRE SFHs are partitioned into their bursty and time-steady phases, the best-fitting FUV time-scale fluctuates from its ~10 Myr value when the SFR is time-steady to $\gtrsim$100 Myr immediately following particularly extreme bursts of star formation during the bursty phase. On the other hand, the best-fitting averaging time-scale for Hα is generally insensitive to the SFR variability in the FIRE simulations and remains ~5 Myr at all times. These time-scales are shorter than the 100 Myr and 10 Myr time-scales sometimes assumed in the literature for FUV and Hα, respectively, because while the FUV emission persists for stellar populations older than 100 Myr, the time-dependent luminosities are strongly dominated by younger stars. Our results confirm that the ratio of SFRs inferred using Hα vs. FUV can be used to probe the burstiness of star formation in galaxies.

Key words: galaxies: star formation – ultraviolet: galaxies – galaxies: high-redshift

1 INTRODUCTION

1.1 Measuring star formation rates observationally

In the regime where counting individual stellar objects and measuring their ages is impossible (e.g. the vast majority of extragalactic systems), star formation rates (SFRs) must be inferred from the observed integrated light from the current stellar population and surrounding ionised gas (Calzetti 2013). Two widely used indicators of star formation are the nebular Hα recombination line (6563 Å) and the far-ultraviolet (FUV) continuum (~1350 − 1750 Å, for the GALEX bandpass). Hα photons, primarily produced in the HII regions surrounding young massive stars, have long been used as an indicator of recent (~10 Myr) star formation due to the short lifetimes of the stars that produce them. On the other hand, older (but still relatively young) stellar populations with masses above ~5 M$_\odot$

dominate the integrated spectrum in FUV and are thought to trace star formation on longer-time-scales (up to ~100 Myr) (Kennicutt & Evans 2012; Calzetti 2013). SFR indicators can thus be thought of as a convolution of the intrinsic "true" star formation history (SFH) with a time-delayed response function. One can take advantage of this fact by combining observations of different SFR indicators to measure SFRs averaged over different times in a galaxy's recent history (e.g., Weisz et al. 2012; Domínguez et al. 2015; Sparre et al. 2017).

There is a vast literature seeking to predict the properties of simple stellar populations (SSPs, notable examples include Leitherer et al. 1999; Bruzual & Charlot 2003; Conroy et al. 2009; da Silva et al. 2012; Eldridge et al. 2017). These SSPs model the evolution of populations of stars from a distribution of zero-age main sequence (ZAMS) masses, known as an initial mass function, or IMF (see Kroupa et al. 1993 for one such example). SSPs make predictions for a number of important and useful properties of the populations, including: their spectral energy distributions

---

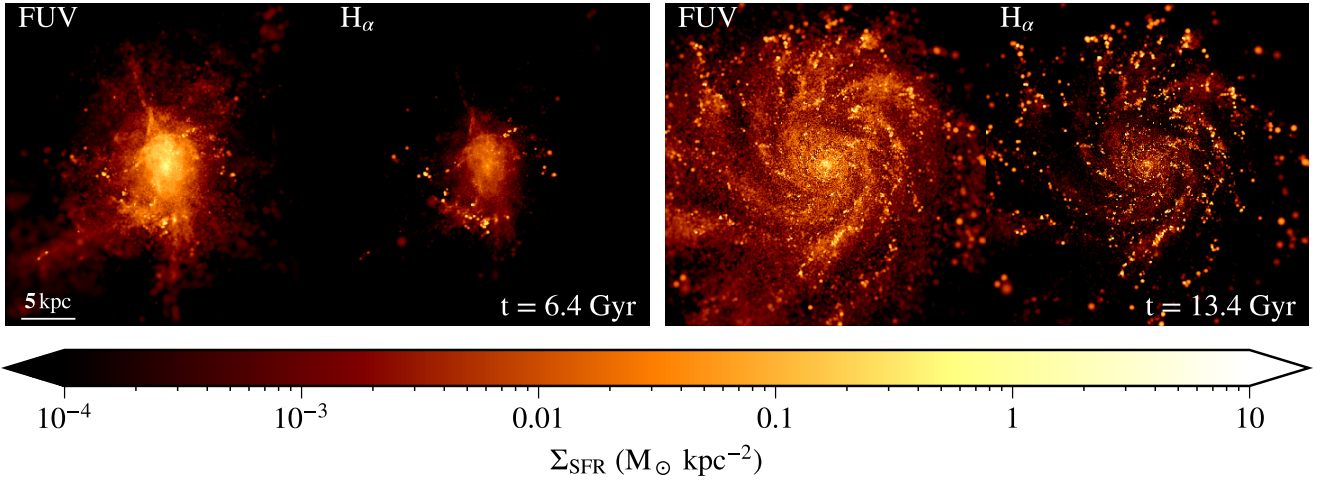⋆ Corresponding author. Email: agurvich@u.northwestern.edu

Figure 1. Star formation rate surface density maps as traced by unattenuated FUV and Hα emission for a simulated Milky Way-mass galaxy (`m12i`) at cosmic time $t = 6.4$ Gyr ($z = 0.9$, $\approx$50 Myr after a burst of star formation; left) and at $t = 13.8$ Gyr ($z = 0.03$, long after the SFR has settled to a steady state; right). The high-redshift panels on the left showcase the irregular morphology of the galaxy during the period of bursty star formation. The larger integrated FUV-indicated SFR also shows how the FUV-indicated SFR following a burst of star formation overestimates the more recent SFR indicated by Hα. In contrast, in the low-redshift panels on the right, which exhibit a well-ordered disk (viewed face-on) after the galaxy's transition to time-steady star formation, have more similar total FUV- and Hα-indicated SFRs. In these unattenuated maps, the Hα light is more concentrated in young, bright star-forming regions, while there is more diffuse FUV light between spiral arms.

(SEDs), supernova rates, distributions of stellar type, estimates of metal yields, distributions of surviving stellar masses, distributions of colours,and both ionising photon rates and narrowband FUV continuum emission as a function of age. The last two of these are the most relevant for the analysis presented here – because they are the basis for the SFR response functions mentioned above.

Once a luminosity response function is determined, the next step is to calibrate a star formation rate indicator by modeling a simple stellar population and the luminosity it emits. Thus, calibration requires making some assumption about the shape of the (recent) SFH. A common choice is a constant SFR, for which the calibration is the asymptotic luminosity of the population formed at that SFR (e.g. Buat et al. 2012; Kennicutt & Evans 2012). When suggested by observations (e.g., constrained by ratios of indicators that act on different time-scales) a "constant burst" (i.e. a top hat of varying width) is sometimes used (e.g. Calzetti et al. 2007; Murphy et al. 2011; Hao et al. 2011). The appropriate calibration in this case (to recover the burst SFR), is the ratio of the luminosity of the stellar population formed during the burst at the inferred time delay of the observation (typically shortly following the burst) to the burst SFR.

A common definition for the time-scale that an indicator acts on is the time that it takes for the calibration population to reach $\sim$90% of its integrated luminosity. Following this definition, the FUV emission is thought to trace stars formed over the past $\sim$100 Myr (Murphy et al. 2011), whilst Hα emission trace stars formed in the past $\sim$10 Myr (Hao et al. 2011). However, since even a stellar population formed in a single burst can emit significant UV light long after its FUV or Hα emission peaks, the 90% "persistence times" can be substantially longer than the SFR time-scales to which FUV and Hα light are sensitive. Moreover, the assumption of a constant SFH (or a single top-hat burst) is not necessarily accurate in real galaxies, which have can have complex and often "bursty" SFHs. Thus, to properly interpret the SFRs implied by common observational indicators, we must understand the time-scales the

indicators probe when applied to realistic SFHs, which may include highly time-variable periods.

1.2 The need to consider 'bursty' star formation

Deviations in the "indicated" (or "measured") SFR from the "true" instantaneous (or "intrinsic") SFR can be substantial when the SFR changes on time-scales shorter than the maximum lifetime of stars that contribute non-negligibly to the observed photons. So-called "bursty" star formation is both a generic prediction of simulations of galaxy formation that include explicitly resolved star-forming regions and stellar feedback (Governato et al. 2012; Teyssier et al. 2013; Hopkins et al. 2014; Agertz & Kravtsov 2015; Sparre et al. 2017; Faucher-Giguère 2018) and is also well-motivated observationally (e.g. Weisz et al. 2012; Smit et al. 2016; Guo et al. 2016; Emami et al. 2019; Hirtenstein et al. 2019; Pelliccia et al. 2020). Specifically, observations use the ratio of short and long time-scale tracers of SFR (e.g. the Hα-to-UV ratio) as a signature of bursty star formation. Since immediately after a burst of star formation the short-time-scale tracer decreases faster than the long-time-scale one, a burst leads to a ratio <1 (unequal dust attenuation could also affect the Hα-to-UV ratio and must also be taken into account, e.g. Koyama et al. 2019; Salim & Narayanan 2020). For example, Weisz et al. (2012) observed a decreasing Hα-to-UV ratio with decreasing galaxy mass, suggesting that bursty star formation is more prevalent in dwarf galaxies (these results are echoed by Guo et al. 2016, who use Hβ instead of Hα). There is also evidence of common SFR variability at high redshift, e.g. in the form of "extreme emission-line galaxies," which have been interpreted as having recently experienced intense starbursts of duration $\sim$15 Myr (van der Wel et al. 2011; Forrest et al. 2017).

Understanding the prevalence and properties of bursty SFHs is of major importance for understand how galaxies form and evolve. The SFR − stellar mass (M_*) relation (also known as the "star for-
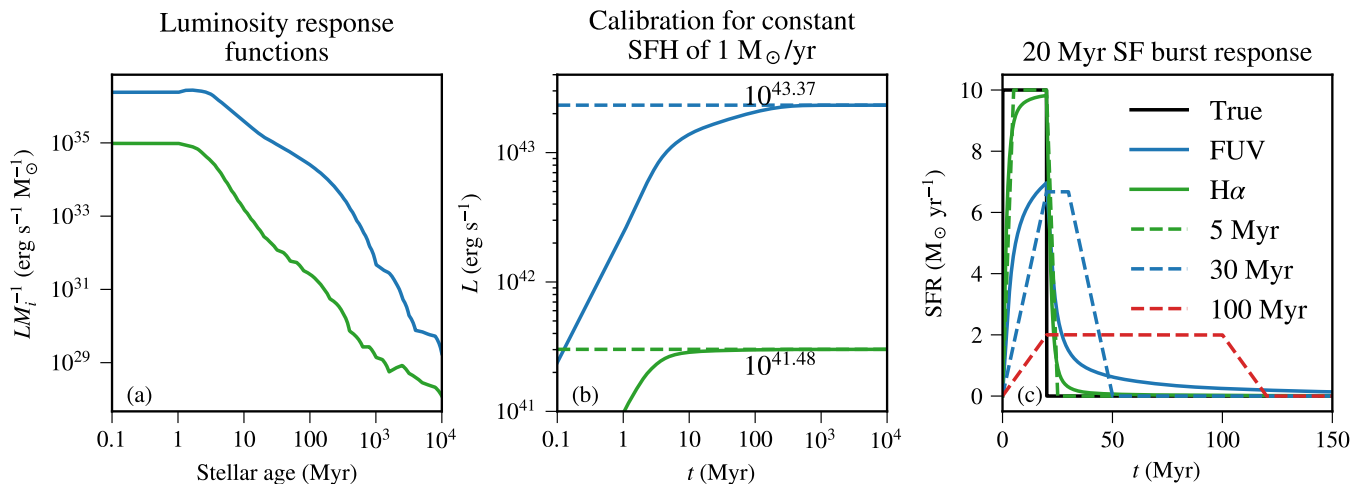
Figure 2. *(a):* Luminosity (per stellar mass formed) following a star formation burst in the FUV continuum and Hα as a function of stellar age, based on a BPASS stellar population synthesis model. *(b):* Evolution of $L_{\rm FUV}$ and $L_{\rm H\alpha}$ as a function of time assuming a SFH with a constant SFR of 1 M$_\odot$ yr^{-1}. SFR indicator calibration constants are defined as the asymptotic luminosity in each case, represented by dashed lines and annotated on each curve. *(c):* Indicated SFR response to a population of stars formed in a 20 Myr burst (solid black line). Coloured dashed lines show moving boxcar averages of the true SFR using different widths: 5 Myr (green), 30 Myr (blue), and 100 Myr (red).

mation main sequence"; Brinchmann et al. 2004; Noeske et al. 2007; Elbaz et al. 2007; Whitaker et al. 2012; Salim et al. 2014; Shivaei et al. 2015; Schreiber et al. 2015) suggests that galaxies form most of their stars in a steady process. However, as summarized above, simulations and observations both indicate that many galaxies undergo short starbursts, during which they lie well above this relation (see e.g. Willett et al. 2015; Sparre et al. 2017; Elbaz et al. 2018; Matthee & Schaye 2019). In detail, it is therefore possible that many galaxies frequently move above and below the mean SFR − M_* relation, rather than evolving smoothly along it (e.g. Orr et al. 2017). The scatter in the observed relation should then reflect, in part, the burstiness of star formation in galaxies. In particular, Sparre et al. (2017) compares the scatter in the observed SFR − M_* relation to simulations from the FIRE (Feedback in Realistic Environments) project[1] and find that, to first order, the time-variability of the SFHs in the simulations is consistent with the observed scatter in SFR − M_* (although some quantitative differences may remain to be explained).

Understanding the time-scales probed by SFR indicators is also relevant for observations outside the UV and for the interpretation of galaxies expected to deviate strongly from the main sequence, e.g. during or following major mergers. Using simulations of merging galaxies combined with detailed radiative transfer, Hayward et al. (2014) showed that the total infrared (IR) luminosity (when interpreted using standard assumptions)[2] over-estimates the true SFR immediately after the merger-induced star formation burst. For major mergers in which a strong starburst is induced, the SFR inferred from the IR luminosity can overestimate the instantaneous SFR during the post-starburst phase by greater than two orders of magnitude.

1.3 This paper

In this paper, we ask the following questions: (1) What are the SFR time-scales probed by Hα and FUV indicators when taking into account realistic SFHs; and (2) how do the results depend on SFR burstiness? To answer these questions, we use SFHs from the FIRE-2 simulations of galaxy formation. We also use the detailed datasets provided by the simulations to assess how the indicated SFR time-scales depend on redshift and galaxy mass. Since our analysis models the application of standard SFR indicators on the simulated SFHs, the results will inform the interpretation of both past and future observational SFR measurements.

The FIRE-2 simulations are the second generation cosmological, zoom-in hydrodynamic simulations from the FIRE project (Hopkins et al. 2014, 2018). These high-resolution simulations include a detailed model for star formation and stellar feedback and produce galaxies that match a number of observed properties, which motivates their use as models for "realistic" SFHs. The properties include the M_*−halomass (M_h relation), mass-metallicity relations (Ma et al. 2016a), the Kennicutt-Schmidt (KS) relation (Hopkins et al. 2014; Orr et al. 2018), and constraints on galactic winds from observations of the circumgalactic medium (e.g., Faucher-Giguère et al. 2015, 2016; Hafen et al. 2017).

Notably for our purposes, the FIRE simulations predict two main phases of star formation: bursty and time steady (e.g., Muratov et al. 2015; Faucher-Giguère 2018). At low redshift, ∼ Milky Way-mass galaxies form long-lived stable disks with time-steady SFR (e.g., Gurvich et al. 2020). At high redshift, the progenitors of these galaxies have much more irregular morphologies and time-variable star formation histories (see e.g. Sparre et al. 2017; Ma et al. 2017; Stern et al. 2020). Figure 1 illustrates the different morphologies predicted in the bursty and steady phases through the lens of the SFR indicators (FUV and Hα light, uncorrected for dust obscuration). The left panels ($z = 0.9$) feature a clumpy and amorphous distribution of star formation while the right panels ($z \sim 0$) show coherent spiral patterns in the same galaxy but at a later time. In the FIRE simulations, star formation typically remains bursty until $z = 0$ in dwarf galaxies.

---

[1] FIRE project website: http://fire.northwestern.edu
[2] Since IR light is produced by reprocessing of UV light by dust, it is expected to probe time-scales similar to FUV.

The remainder of the paper is organised as follows. In §2 we describe the simulations in more detail, as well as how we define and analyze SFR indicators. In §3 we infer the best-fitting averaging time-scales as a function of cosmic time in galaxies of different masses. We discuss our results in §4 and in §5 we summarise and conclude.

2   METHODS

2.1   Star formation histories from FIRE-2 simulations

The FIRE-2 simulations are cosmological zoom-in simulations run in the Meshless Finite Mass (MFM) mode of the GIZMO gravity+magnetohydrodynamic code.[3] MFM is a Lagrangian, mesh-free, finite-mass method combining the advantages of traditional smooth particle hydrodynamics and grid-based methods (for numerical details and tests, see Hopkins 2015). The FIRE-2 physics model, which is described in full detail in Hopkins et al. (2018), includes radiative cooling for gas down to 10 K (including approximate treatments of fine-structure metal and molecular lines). Star particles representing simple stellar populations are formed in gas that is self-gravitating, dense ($n_H \geq 1000$ cm^{-3}), and molecular (Hopkins et al. 2013). Star particles return mass, metals, momentum, and energy in the interstellar medium (ISM), at rates that are functions of the star particle's age following the STARBURST99 population synthesis model (Leitherer et al. 1999). Stellar feedback is modeled on the scale of star-forming regions and includes supernovae (Type II and Ia), stellar winds from O, B, and AGB stars, photoelectric heating, photoionization, and radiation pressure.

We study analyze a range of galaxy masses, from dwarf galaxies up to ∼$L^\star$. This allows us to study the different types of SFHs experienced by star-forming galaxies. We analyze eight simulations in total: four dwarfs with $z = 0$ halo mass in the range $M_h \sim 10^9 - 10^{11}$ M$_\odot$ and four galaxies with halo mass $M_h \sim 10^{12}$, similar to the Milky Way. Table 1 catalogs some basic physical properties of these galaxies at redshift $z = 0$. The mass of baryonic resolution elements ranges from $m_b \approx 250$ $M_\odot$ (for dwarfs) to ≈7100 $M_\odot$ (for the m12 galaxies). More details on resolution and other facets of the FIRE-2 simulations are given in Hopkins et al. (2018) and Garrison-Kimmel et al. (2017, 2019). All simulations include a sub-grid model for turbulent metal diffusion between nearby gas cells.

We use an "archaeological" approach to reconstruct the SFHs of the galaxies in the FIRE simulations at high time resolution. Specifically, we first identify all of the stars in the galaxy's main halo at redshift $z = 0$. To do so, we use the AMIGA halo finder (Gill et al. 2004; Knollmann & Knebe 2009) to locate the main halo in our simulation volume and measure the virial radius (R_{vir}) and the halo centre of mass (measured using all of the dark, gas, and stellar components of the galaxy). Dark matter haloes are defined using the Bryan & Norman (1998) redshift-dependent overdensity criterion. We extract the star particles within a spherical volume of radius $5R_{*,half}$, where $R_{*,half}$ is the radius containing 50% of the stars inside $0.15R_{vir}$. The time-dependent SFH is then reconstructed from the distribution of star particle formation times (SFTs) and star masses, self-consistently accounting for stellar mass loss. This archaeological approach neglects the fact that some stars formed in galaxies other than the main progenitor (and then merged), but this

Table 1. Properties at $z = 0$ of the simulated galaxies analyzed in this paper.

Name	M_h $(M_\odot)$[a]	M_* $(M_\odot)$[b]	$R_{*,half}$ (kpc)[c]	f_g[d]
m10q	7.7×10^9	2.3×10^6	0.8	0.68
m11i	6.8×10^{10}	1.0×10^9	3.7	0.61
m11q	1.4×10^{11}	6.5×10^8	2.5	0.67
m11d	2.7×10^{11}	4.5×10^9	6.9	0.57
m12i	9.4×10^{11}	6.8×10^{10}	2.9	0.20
m12b	1.1×10^{12}	9.0×10^{10}	2.8	0.16
m12c	1.1×10^{12}	6.4×10^{10}	3.4	0.22
m12f	1.3×10^{12}	8.8×10^{10}	4.0	0.24

[a] Total dark matter and baryonic mass within R_{vir}, the virial radius defined as in Bryan & Norman (1998).
[b] Total stellar mass within $5R_{*,half}$.
[c] 3D radius containing half of the total stellar mass within 15% of R_{vir}.
[d] Gas fraction $f_g = M_g/(M_* + M_g)$, where M_g is the gas mass within the galaxy.

is a good approximation for galaxies up to ∼$L^\star$, which form most of their stars *in situ* (e.g., Anglés-Alcázar et al. 2017; Fitts et al. 2018).

From this high time-resolution SFH, we can construct SFHs with the SFR boxcar-averaged on an arbitrary time-scale t_{avg}, which we denote $\langle SFR_{true}\rangle_{t_{avg}}(t)$. Since, in observational applications, only the SFR before the time of observation is well defined, we define these boxcar averages by averaging the *preceding* t_{avg} time interval preceding a given cosmic time t. Figure 3 shows the SFH for one representative simulation in each mass bin.

For each galaxy, we identify the "end" of bursty star formation by computing the root mean square relative error (RMSRE) in log-space using a 500 Myr-wide moving boxcar :

$$RMSRE_{SFH} = \sqrt{\frac{\langle \log_{10}(SFR)^2\rangle_{500\,Myr} - \langle \log_{10}(SFR)\rangle^2_{500\,Myr}}{\langle \log_{10}(SFR)\rangle^2_{500\,Myr}}}.$$
(1)

To account for periods when the SFR is identically zero, we add one tenth of the minimum true SFR to the entire SFH (this choice does not affect any of our results). We consider the SFH to become "steady" when $RMSRE_{SFH} \leq 0.3$. The bottom panel of Figure 3 shows an example of this metric applied to the m12i simulation and how it accurately identifies the clear change in SFR behavior in this case. Dwarf galaxies in FIRE are typically bursty all the way to $z = 0$, so no transition is identified for these galaxies.

2.2   Star formation rate indicators

We model stellar spectra as a function of age using version 2.2.1 of the Binary Population and Spectral Synthesis (BPASS) stellar population synthesis code (Eldridge et al. 2017). BPASS models the effects of binary evolution on stellar spectra and uses CLOUDY (Ferland et al. 1998) to compute nebular emissions, which is the main contributor to Hα emission.[4] We use a fixed BPASS model, which consists of a Kroupa IMF (Kroupa et al. 1993) with a metallic mass fraction of $Z = 0.014$. To derive observationally-indicated

---

[3] Information about GIZMO and a public version of the code are available at: https://www.tapir.caltech.edu/~phopkins/Site/GIZMO.

[4] The STARBURST99 stellar population synthesis model used for the FIRE feedback model does not include binaries. As in previous work with BPASS (e.g., Ma et al. 2016b), we neglect possible dynamical differences (during the hydrodynamic simulations) between the different stellar evolution models but include the spectral differences which are most directly relevant to the present study.
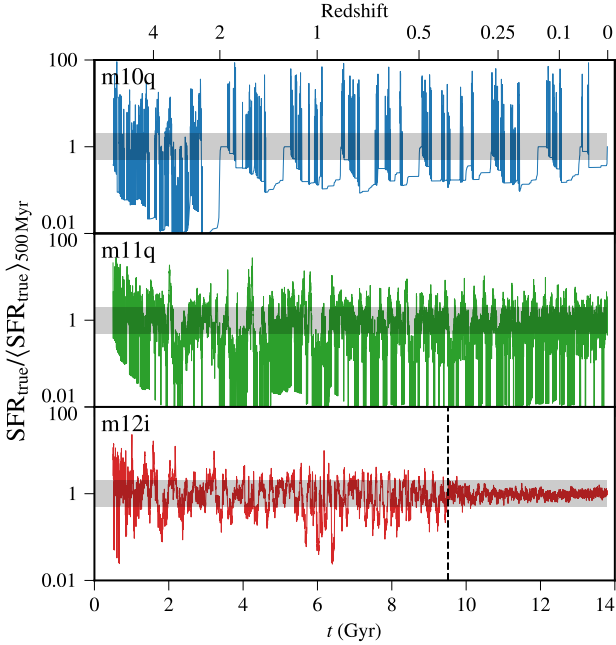
Figure 3. Star formation histories of three prototypical galaxies from our simulation sample, one from each halo mass bin considered (m10q, halo mass $M_h \sim 10^{10}$ M$_\odot$ at $z = 0$; m11q, $M_h \sim 10^{11}$ M$_\odot$; m12f, $M_h \sim 10^{12}$ M$_\odot$). In each panel, the SFR is normalized by the 500 Myr running boxcar-averaged SFR. Dwarf galaxies (top two panels) have bursty SFHs at all redshifts. Milky Way-mass galaxies with $M_h(z = 0) \sim 10^{12}$ M$_\odot$ (bottom panel) undergo a transition from a bursty SFR at high redshift to a time-steady SFR at low redshift (with some remaining, but much smaller fluctuations). The transition from bursty to steady SFR is indicated by the vertical black dashed line in the bottom panel. Shaded regions show a factor of 0.3 dex in either direction of unity.

SFR values, SFR$_{\rm FUV}$ and SFR$_{\rm H\alpha}$, we average the specific BPASS FUV flux over the wavelength interval 1556-1576 Å (near the center of the GALEX FUV channel) and use the Hα flux modeled by BPASS. This results in stellar age-dependent "response functions," shown in Figure 2a.

In order to convert the modeled ("observed") luminosity into an indicated star formation rate, we assume a constant light-to-SFR ratio, i.e.

$$\mathrm{SFR}_{\rm ind} = C^{-1} L_{\rm ind} \qquad (2)$$

where C is the SFR "calibration constant." This constant can be determined by considering the asymptotic luminosity, $L_{\rm ind}(t \to \infty)$, of a population of stars forming at a constant rate of SFR$_{\rm ind}$. These calibration constants neglect obscuration by dust, which should be accounted for when attempting to measure the SFR of real galaxies. In principle, one can relax the assumption of time-constant SFR. In §3.2 we quantify the expected errors in indicated SFRs (relative to true SFRs), assuming that real SFHs are well modeled by the FIRE-2 simulations we analyze.

Figure 2b shows $L_{\rm ind}$ as a function of time for SFR$_{\rm true}(t) = 1$ M$_\odot$ yr^{-1}. For the FUV continuum, $L_{\rm ind} = \nu \langle L_\nu \rangle$ is evaluated at the middle of the FUV wavelength sample (1566 Å). Using Equation (2), we find calibration constants of $C_{\rm FUV} = 10^{43.33}$ erg s^{-1}/M$_\odot$ yr^{-1} and $C_{\rm H\alpha} = 10^{41.42}$ erg s^{-1}/M$_\odot$ yr^{-1}.

We note that each indicator reaches $L_{\rm ind} \simeq 0.9 L_{\rm ind}(t \to \infty)$ at $t \approx 100$ Myr and $t \approx 10$ Myr respectively– the often quoted time-scales for each of these indicators.

Figure 2c shows the SFR response of these indicators applied to a population of stars formed by a 20 Myr burst of star formation at 10 M$_\odot$ yr^{-1}, beginning at $t = 0$. We compare the indicated SFRs to three moving "boxcar" averages of width 5, 30, and 100 Myr. One important takeaway is that the 100 Myr running average is a poor match to the FUV indicated SFR at all times, which hints that the "effective" FUV response time-scale is much shorter. On the other hand, the 5 Myr average agrees well with the Hα indicated SFR.

2.3 Inferring the time-scales of SFR indicators

Next, we compare the true SFH to the "indicated" SFHs using the calibrated indicators from §2.2. To measure the indicated SFR$_{\rm ind}(t)$ (i.e., the SFR that would be inferred using a standard observational indicator, as defined in the previous section), we consider the total luminosity from the stars in a galaxy with SFT$< t$, i.e.

$$\mathrm{SFR}_{\rm ind}(t) = C_{\rm ind}^{-1} \sum_{i, \ \mathrm{SFT}_i < t} L_{\rm ind}^i (t - \mathrm{SFT}_i), \qquad (3)$$

where $L_{\rm ind}^i(t - \mathrm{SFT}_i)$ corresponds to the response functions in Figure 2a, evaluated for star particle i with a stellar age $(t - \mathrm{SFT}_i)$.

Our methodology for comparing the true and indicated SFRs is illustrated in Figure 4. At any given time there is, in general, a non-zero deviation between the true and indicated SFRs The goal of our analysis is to identify the *best-fitting boxcar averaging time-scale*, $t_{\rm avg}^{\rm min}$, that minimises this difference between $\langle \mathrm{SFR}_{\rm true} \rangle_{t_{\rm avg}}$ and a given SFR$_{\rm ind}$. Physically, $t_{\rm avg}^{\rm min}$ is the width of the boxcar over which one would have to average the true SFR to match the indicated SFR at the time of an observation.

When the SFH fluctuates rapidly, many $t_{\rm avg}$ may produce the same $\langle \mathrm{SFR}_{\rm true} \rangle_{t_{\rm avg}}$ that match the indicated SFR. To avoid this issue, we determine best-fitting $t_{\rm avg}^{\rm min}$ for *ensembles of observation times* in windows of size $T_{\rm w} = 500$ Myr (longer that the typical short time-scale variations during bursty phases). The increased accuracy in $t_{\rm avg}^{\rm min}$ resulting from introducing the time window comes at the cost of decreased ability to localise $t_{\rm avg}^{\rm min}$ in time within the window. We assign best-fitting values of $t_{\rm avg}^{\rm min}$ to the end of time windows (rather than the middle, for example). This ensures that $t_{\rm avg}^{\rm min}$ is computed using only SFRs that are causally connected to the observation time t. We quantify how our results depend the exact choice of $T_{\rm w}$ in Appendix A and find that they are stable for our fiducial choice of $T_{\rm w} = 500$ Myr.

To find the best-fitting $t_{\rm avg}^{\rm min}$, we define another root mean square error which is a function of $t_{\rm avg}$:

$$\mathrm{RMSE}(t_{\rm avg}) = \sqrt{\frac{\sum_i \left(\log_{10} \mathrm{SFR}_{\rm ind}^i - \log_{10} \langle \mathrm{SFR}_{\rm true} \rangle_{t_{\rm avg}}^i \right)^2}{n}}, \quad (4)$$

where i is a sum over time samples spaced by 1 Myr covering the time window of total width $T_{\rm w}$. This corresponds to the scatter with respect to the one-to-one line in log-space in the middle row of Figure 4. Within a given time window, we repeat this process and recompute SFHs of $\langle \mathrm{SFR}_{\rm true} \rangle_{t_{\rm avg}}$ varying $1 \le t_{\rm avg} \le 1000$ Myr in steps of 1 Myr (see the bottom row of Figure 4). Lastly, we define the global minimum of this curve as $t_{\rm avg}^{\rm min}$. We repeat this procedure in ~13000 maximally overlapping windows (i.e. overlapping by 499 Myr) in order to construct histories of $t_{\rm avg}^{\rm min}$ over cosmic time. We
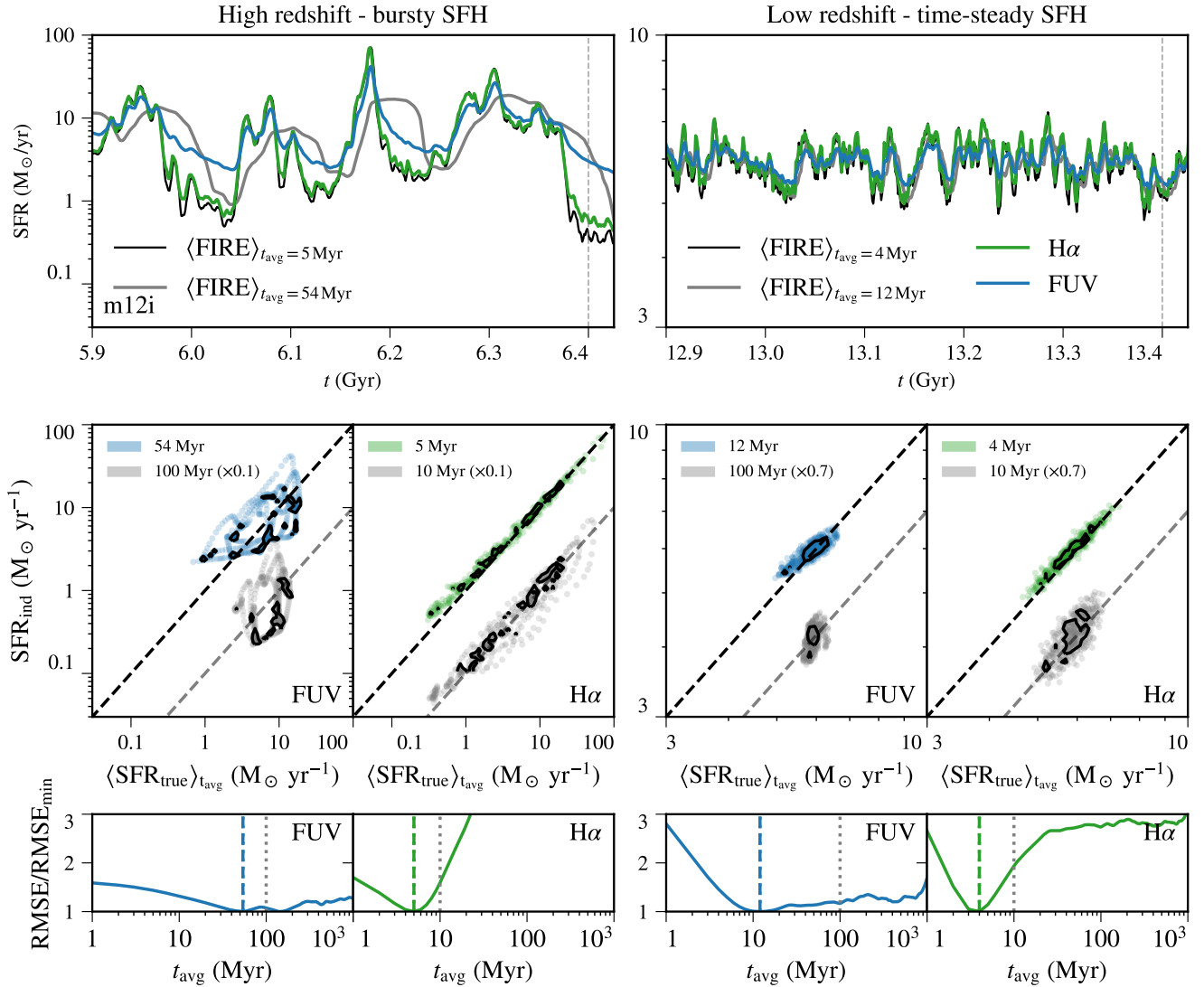
Figure 4. *Top:* "True" and "indicated" SFHs in a 500-Myr window at high (left) and low (right) redshift in `m12i`. True SFHs are plotted using best-fitting, boxcar-average equivalent time-scales for FUV (grey) and Hα (black). Grey vertical lines are plotted to identify the times corresponding to the renderings in Figure 1. At early times the SFR frequently changes by a factor of > 10 on time-scales ~30 − 50 Myr while at late times it varies only by ≲10%. *Middle:* Scatter plot of the indicated star formation rate, SFR_{ind}, vs. the true star formation rate, boxcar-averaged using the best-fitting averaging time-scale (coloured). Contours containing 50% of the points are plotted in black alongside a dashed line showing along the one-to-one relation. For comparison, scatter plots for SFR boxcar-averaged over time-scales of 100 Myr and 10 Myr are also shown in grey in the FUV and Hα panels, respectively (offset vertically by the factors noted on the figure for visual clarity). The smaller scatter in the colored points vs. the grey is visible by eye in all four panels. *Bottom:* Root mean square error (RMSE) between the indicated and time-averaged true SFHs as a function of boxcar averaging time-scale t_{avg}, normalized by the minimum RMSE. Vertical dashed lines (coloured) are plotted at the locations of the minima, while the dotted (grey) vertical lines indicate 100 Myr and 10 Myr time-scales for reference. At both early and late times, Hα has a well-defined minimum RMSE in almost all time windows. For FUV, on the other hand, the RMSE curve is typically much shallower, especially in the bursty high-redshift regime, implying that the equivalent boxcar average time-scale is not as well defined. Note that the value of t_{avg}^{min} inferred in the high-redshift window shown here is not necessarily representative since the best-fitting time-scale fluctuates strongly following particularly extreme bursts of star formation like the one shown here (see Figure 5).

omit the first 1 Gyr of the simulation to exclude transient effects related to the initial formation of the dark matter halo and galaxy.

3   RESULTS

3.1   Best-fitting time-scales

Figure 4 summarises our key results for two $T_w = 500$ Myr windows in `m12i`, a representative simulation of a Milky Way-mass halo. The left column focuses on high-redshift period, when the star formation is bursty, while the right column focuses on a low-redshift period when the SFR is relatively time-steady. The top row shows the SFHs
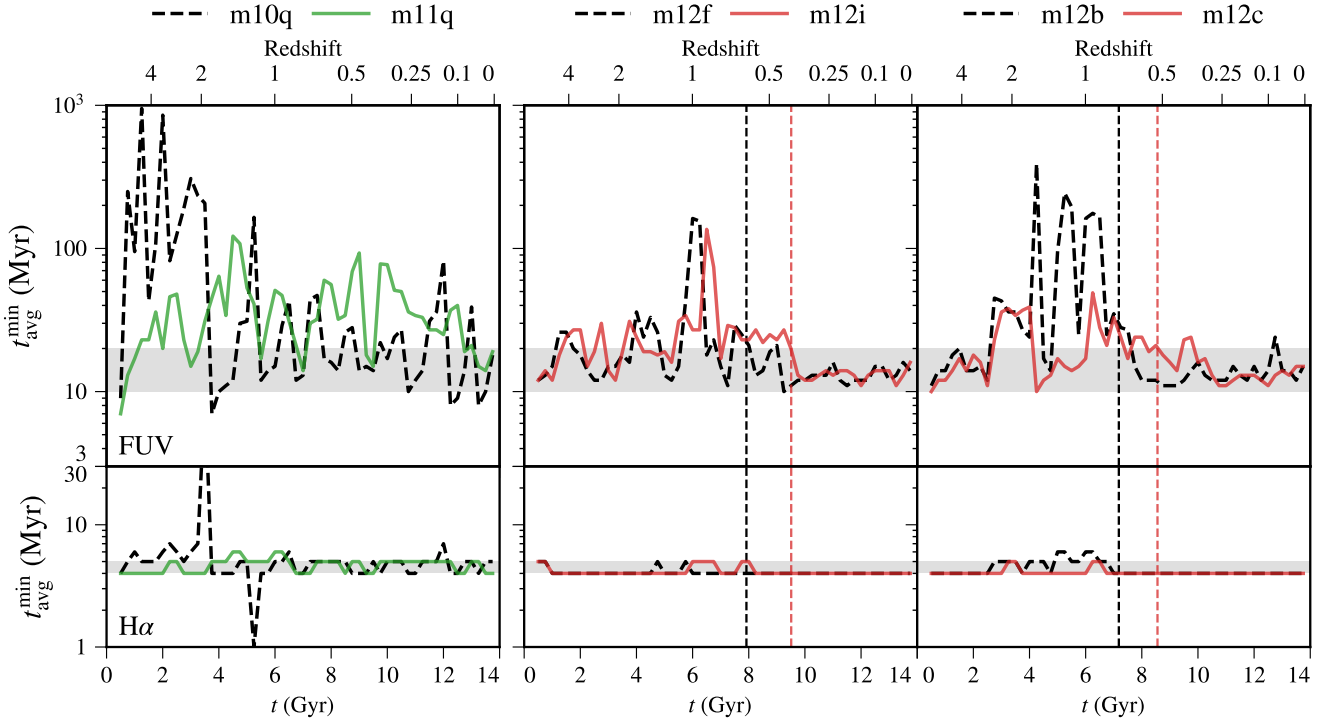
Figure 5. Best-fitting boxcar-average equivalent time-scale, $t_{\mathrm{avg}}^{\min}$, for both FUV (top) and Hα (bottom) for different simulations as a function of cosmic time. Grey shaded regions are shown to help identify departures from the time-scales we identify in the time-steady limit for each indicator ($10-20$ Myr for FUV and $4-5$ Myr for Hα). *Left*: Simulations with halo mass $M_h \sim 10^{10}$ M$_\odot$ and $M_h \sim 10^{11}$ M$_\odot$ at $z = 0$. *Middle and Right*: Simulations with $M_h \sim 10^{12}$ M$_\odot$. The simulations of Milky Way-mass galaxies with $M_h \sim 10^{12}$ M$_\odot$ experience a transition from bursty to time-steady SFR at the time indicated by the vertical dashed lines. For time periods when the SFR is bursty (regardless of halo mass) the best-fitting averaging time-scale for FUV fluctuates strongly and reaches much higher values than for time periods when the SFR is time-steady. For Hα, the shorter best-fitting averaging time-scale $4-5$ Myr is generally stable and insensitive to the shape of the SFH.

during these periods. At early times (left panel) the SFR changes by a factor of >10 on time-scales of $\sim 30-50$ Myr whereas at late times (right panel) the SFR changes only by $\lesssim 10\%$.

The middle-row panels show scatter plots of the true SFRs averaged over the best-fitting averaging time-scale, $t_{\mathrm{avg}}^{\min}$, vs. the indicated SFRs for FUV and Hα for the times corresponding to the right edge of the top-row panels. We also plot indicated SFHs for the often-quoted time-scales associated with each indicator (100 Myr and 10 Myr), rather than $t_{\mathrm{avg}}^{\min}$, for comparison in gray. The points for the 100 Myr and 10 Myr time-scales are offset vertically for clarity (by factors indicated on the panels). Contours containing 50% of points in each case are shown in solid black. We see that the scatter for $t_{\mathrm{avg}}^{\min}$ is substantially smaller than the scatter for the reference 100 Myr and 10 Myr time-scales.

The bottom row of Figure 4 shows the RMSE as a function of t_{avg}, defined in Equation (4), normalised by the RMSE at $t_{\mathrm{avg}}^{\min}$ (the RMSE minimum). We see little difference between the $t_{\mathrm{avg}}^{\min}$ for Hα when comparing the high- and low-redshift results (5 Myr vs. 4 Myr). This is because Hα probes time-scales over which the SFR does not change drastically even in the bursty regime. Thus, Hα tracks the true, instantaneous SFR fairly accurately in both the bursty and steady regimes.

FUV, on the other hand, shows more dependence on the burstiness of SFR. For the example shown in the right column of Figure 4, when SFR is time-steady, we find a best-fit $t_{\mathrm{avg}}^{\min} \approx 12$ Myr. This is

in contrast to the much longer best-fit $t_{\mathrm{avg}}^{\min} \approx 54$ Myr for the bursty period on the left experienced earlier by the same galaxy. As we discuss in more detail below, the best-fit $t_{\mathrm{avg}}^{\min}$ can fluctuate strongly immediately following particularly extreme bursts of star formation, so the best-fit for this example is not necessarily representative.

A concrete example of how FUV responds to a strongly changing SFR is shown in the top left panel of 4 (see the vertical dashed line at $t = 6.4$ Gyr). The left panels of Figure 1 show renderings of the FUV and Hα light from the galaxy at this time. In this case, due to the strong drop in SFR shortly before the $t = 6.4$ Gyr "observation time," the observed FUV light was emitted from stars that formed $\sim 50-100$ Myr in the past. As a result, the FUV-indicated SFR is much larger than true instantaneous SFR, so that this indicated SFR is more representative of a time-average extending to when the stars dominating the observed emission formed.

Next, we explore how $t_{\mathrm{avg}}^{\min}$ varies as a function of cosmic time and galaxy mass. Figure 5 shows the evolution of $t_{\mathrm{avg}}^{\min}$ for FUV and Hα over cosmic time for m10q, m11q, and all four m12 simulations listed in Table 1. For clarity, we show only results for a subset of the $\sim$13000 overlapping windows described in §2.3. Specifically, in each panel we show results for 56 equally spaced windows, each overlapping by 250 Myr with its neighbors.

We first focus on the two rightmost columns, corresponding to Milky Way-mass galaxies, which have dark matter haloes of mass $M_h \sim 10^{12}$ M$_\odot$ at $z = 0$ (the m12 simulation plotted in red in the middle column is the same as in Figure 4). These galaxies transition
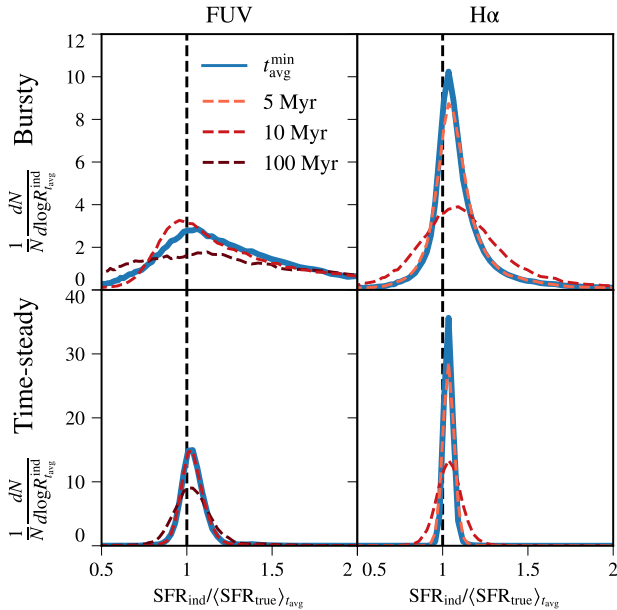
Figure 6. Distributions of the indicated-to-time-averaged-true-SFR ratio, $R_{t_{avg}}^{ind} \equiv SFR_{ind}/\langle SFR_{true}\rangle_{t_{avg}}$, for different averaging timescales, t_{avg}, and SFR indicators (FUV, left column; Hα, right column). SFHs from each simulation listed in Table 1 are partitioned into bursty (top row) and time-steady (bottom row) regimes and then combined to form each distribution plotted. Distributions using t_{avg}^{min} are plotted in blue while different shades of red identify different fixed t_{avg} used to average the true SFR. Vertical dashed lines are plotted at a ratio of unity, while the standard derivations of these distributions in dex are compiled in Table 2. The scatter of the $\log_{10} R_{t_{avg}}^{ind}$ distribution, peaked near unity, is generally smallest for t_{avg}^{min}, though similar to the scatter for the fixed 10 Myr and 5 Myr time-scales for FUV and Hα, respectively.

from bursty at high redshift to steady at later times. Vertical dashed lines indicate the times when bursty star formation ends for each simulation, using the definition in §2.1. We see that, when the SFR is time-steady (to the right of the dashed lines), the best-fitting averaging time-scales for Hα and FUV are relatively stable (especially for Hα) at $4-5$ Myr and $10-20$ Myr, respectively. These ranges are indicated by the shaded regions in each row. As we found for the example in Figure 4, the best-fit t_{avg}^{min} for Hα is, in most cases, nearly the same even at high redshift when SFRs are highly variable. However, the best-fit t_{avg}^{min} for FUV fluctuates strongly in time, by factors up to > 10 (i.e., up to values $t_{avg}^{min} > 100$ Myr). Thus, during bursty periods there is a large uncertainty in the actual time-scales probed by FUV-indicated SFRs.

The left column of Figure 5 shows the results for dwarf galaxies in haloes of $z = 0$ mass $M_h \sim 10^{10}$ M$_\odot$ and $\sim 10^{11}$ M$_\odot$ (m10q and m11q). The SFHs for these dwarf galaxies are bursty at all times. The more extreme burstiness for these dwarf galaxies (see the SFHs in Figure 3) leads to more frequent excursions to very long values of t_{avg}^{min}. For m10q, the figure shows that values of $t_{avg}^{min} \gg 100$ Myr (up to ~ 1 Gyr) are found at some early times ($z \geq 2$).

3.2 Theoretical uncertainty due to unknown SFH

In the previous section, we quantified the best-fitting time-scales for FUV and Hα indicators in a statistical sense. Even when the relevant

Table 2. Intrinsic[a] 1-σ scatter in $\log_{10}(SFR_{ind}/\langle SFR_{true}\rangle_{t_{avg}})$ for different averaging time-scales in the bursty and time-steady star formation phases

SFR phase	FUV			Hα		
	t_{avg}^{min}	10 Myr	100 Myr	t_{avg}^{min}	5 Myr	10 Myr
Bursty	0.143[b]	0.120[b]	0.242	0.035	0.041	0.094
Time-steady	0.025	0.026	0.042	0.011	0.014	0.030

[a] This neglects uncertainties from observational effects, stellar population synthesis modeling, dust obscuration, etc.
[b] Note that in this case the 10 Myr average produces a scatter smaller than (but similar to) the t_{avg}^{min} average. This is possible because the minimization procedure used to obtain t_{avg}^{min} is different from minimizing the width of the $R_{t_{avg}}^{ind}$ distribution (see §2.3). As a result, the time-scale that minimizes the RMSE in a 500 Myr window is not guaranteed to also minimize the $1-\sigma$ scatter of the corresponding log-ratio distribution (Figure 6). Moreover, stochasticity in the SFH, especially in the bursty regime, can introduce noise in the numerical estimates of scatter.

time-scale is known, an important question is: how well does the indicated SFR match the true SFR boxcar-averaged over t_{avg}^{min} when a measurement is made? In general, $\langle SFR_{true}\rangle_{t_{avg}^{min}} \neq SFR_{ind}$ because, depending on the SFH history, there may be *no* value of t_{avg} for which the indicated SFR exactly matches the boxcar average over the preceding t_{avg}. This introduces a minimum uncertainty (absent other information) in any measurement due to the unknown shape of the recent SFH, on top of the modeling uncertainties associated with the assumed stellar population synthesis model (including the IMF) and dust obscuration.

Figure 6 quantifies this uncertainty by plotting distributions of the indicated-to-time-averaged-true-SFR ratio, $R_{t_{avg}}^{ind} \equiv SFR_{ind}/\langle SFR_{true}\rangle_{t_{avg}}$, for different averaging time-scales t_{avg}. To produce these distributions, we first partition the simulations listed in Table 1 into their bursty and time-steady phases (the two rows in the figure). For each of these phases, we consider the FUV and Hα indicators separately (the two columns). Then, for each panel, we evaluate the ratio $R_{t_{avg}}^{ind}$ for $t_{avg} = t_{avg}^{min}$, 100 Myr, 10 Myr, and 5 Myr at 1 Myr intervals (at each time, t_{avg}^{min} is obtained by minimizing over a time window of total width $T_w = 500$ Myr, as described in §2.3). The distributions are shown for the results from all the simulations combined.

We see that, in almost all panels, t_{avg}^{min} produces the smallest scatter around $R_{t_{avg}}^{ind} \approx 1$, as expected since t_{avg}^{min} is defined as the best-fitting time-scale in each case. The $R_{t_{avg}}^{ind}$ distributions also confirm the results from the previous section that $t_{avg}^{min} \sim 10$ Myr for FUV and $t_{avg}^{min} \sim 5$ Myr for Hα (see Figure 5), since the distributions are similar when using either t_{avg}^{min} or the corresponding constant averaging time-scale. On the other hand, the scatters for $t_{avg} = 100$ Myr and $t_{avg} = 10$ Myr are significantly larger in all panels, indicating again that these time-scales are typically much longer than those effectively probed by either FUV or Hα.

To further quantify the $R_{t_{avg}}^{ind}$ distributions, we compute the standard deviations of $\log_{10} R_{t_{avg}}^{ind}$ for different cases and list the results in Table 2. For comparison, the typical observational uncertainty in SFRs measured through monochromatic indicators, combinations of monochromatic indicators, or SED modeling is $\sim 0.1 - 0.3$ dex (e.g. Hao et al. 2011; Koyama et al. 2015; Iyer et al. 2019). Thus, the 0.12-0.14 dex intrinsic scatter that we predict for FUV in the bursty regime for $t_{avg}^{min} \approx 10$ Myr, due solely to the "unknown" preceding
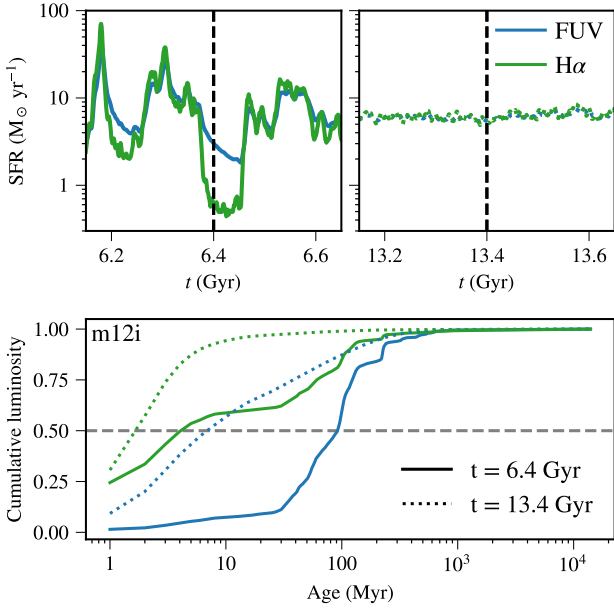
Figure 7. *Top:* SFHs near cosmic-times $t = 6.4$ Gyr ($z = 0.9$ and ≈ 50 Myr after a burst of star formation; left) and $t = 13.4$ Gyr ($z = 0.03$ and long after the SFR has settled to a steady state; right) as indicated by FUV (blue) and Hα (green) for m12i. *Bottom:* Cumulative luminosity in FUV and Hα as a function of stellar age, at $t = 6.4$ Gyr (solid curves) and $t = 13.4$ Gyr (dotted curves). A horizontal dashed line is plotted at 50% to identify the intersection with each cumulative luminosity curve, which we define as $t_{50\%}$ (see §4.1). For FUV $t_{50\%}$ is strongly dependent on the recent SFH and is larger when the SFR is bursty compared to when it is time-steady. For Hα, $t_{50\%}$ also varies depending on the recent SFH but by a smaller factor (~2× in the example shown).

SFH, can be a significant additional source of uncertainty. On the hand, the intrinsic scatters $\approx 0.01 - 0.04$ dex predicted for Hα (in the steady and bursty regimes) for $t_{\text{avg}}^{\text{min}} \approx 5$ Myr imply that this intrinsic uncertainty is usually subdominant.

4 DISCUSSION

4.1 Range of time-scales probed

So far, we have characterized the time-scales probed by SFR indicators by $t_{\text{avg}}^{\text{min}}$, which is the equivalent width of a boxcar-average response kernel. In reality, observational SFR indicators probe light emitted by stars with a range of different ages. This is especially true for FUV light, whose emission persists long after the Hα emission powered by ionizing radiation becomes negligible (e.g., left panel of Figure 2). Another way to characterize the time-scales probed by an indicator is to partition the total luminosity observed at a time t by the age of the stars contributing to the light. At any given cosmic time t, we define $t_{50\%}$ as the stellar age below which the combined luminosity in the band of interest is 50% of the total luminosity, i.e. the light-weighted median stellar age. Similarly, we define t_x for $x = 65\%$, 90% and 95%. These time-scales reflect the extent to which older stars contribute to the observed luminosity compared to younger stars.

Figure 7 illustrates how the total observed luminosity is contributed to by stars of different ages for two different cosmic times
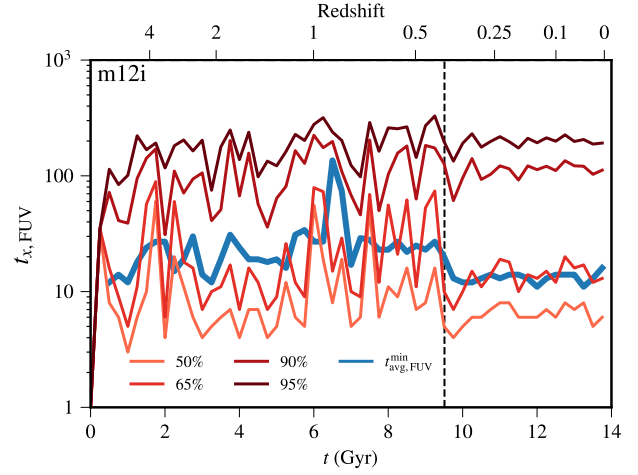

Figure 8. FUV light-weighted percentile stellar ages, t_x, for different percentile values ($x = 50\%, 65\%, 90\%,$ and 95%) as a function of cosmic time in m12i. The best-fitting boxcar-average equivalent time-scale, $t_{\text{avg}}^{\text{min}}$, is also shown for comparison (solid blue), along with the end of bursty star formation (vertical dashed line). Both $t_{\text{avg}}^{\text{min}}$ and t_x fluctuate much more strongly during the bursty phase. The fluctuations can cause the different t_x curves to reach values well above the quasi-steady values predicted at late times, especially, for the smaller percentiles, which are more sensitive to short time-scale SFR fluctuations.

in m12i, one during a period in the bursty phase and one in the time-steady phase. Because the time-scale of Hα is short compared to most SFR variations, it tracks the true SFR with relatively little time delay in either the bursty phase or the steady phase ($t_{50\%} \sim 2 - 4$ Myr). On the other hand, FUV exhibits a much larger difference between the two phases of star formation, with $t_{50\%}$ fluctuating from ~5 Myr to ~ 50 Myr in the bursty phase, before stabilizing in the time-steady phase.

Figure 8 demonstrates in more detail how the stellar age distribution of observed FUV photons fluctuates by comparing $t_{\text{avg}}^{\text{min}}$ to different t_x for m12i as a function of cosmic time. Both $t_{\text{avg}}^{\text{min}}$ and t_x fluctuate much more strongly during the bursty phase (left of the vertical dashed black line) than in the more steady SFR phase (right of the vertical line). The fluctuations can cause the different t_x curves to reach values well above the quasi-steady values predicted at late times. This is especially so for the smaller percentiles, which are more sensitive to short time-scale SFR fluctuations. As expected from previous studies, the asymptotic value of $t_{90\%} \sim 100$ Myr is consistent with the time-scale sometimes associated with FUV, defined such that FUV reach 90% of its asymptotic luminosity for a constant SFR (see §1.1). In general, the distribution and time evolution of $t_{x\%}$ values depend on the details of the SFH, and so can depend on galaxy mass and redshift. However, for all simulations that achieve time-steady SFRs at late-times, the $t_{x\%}$ that best matches the late-time $t_{\text{avg}}^{\text{min}}$ is $t_{65\%}$.

4.2 Hα-to-FUV ratio as a gauge of SFR burstiness and its relation to $t_{\text{avg}}^{\text{min}}$ and $t_{50\%}$

Since FUV and Hα probe the SFR averaged over different time-scales, the ratio of FUV to Hα can be used as a probe the SFR variability (e.g., Fumagalli et al. 2011; Weisz et al. 2012). As the best-fit time-scales $t_{\text{avg}}^{\text{min}}$ and $t_{50\%}$ are also sensitive to changes in the
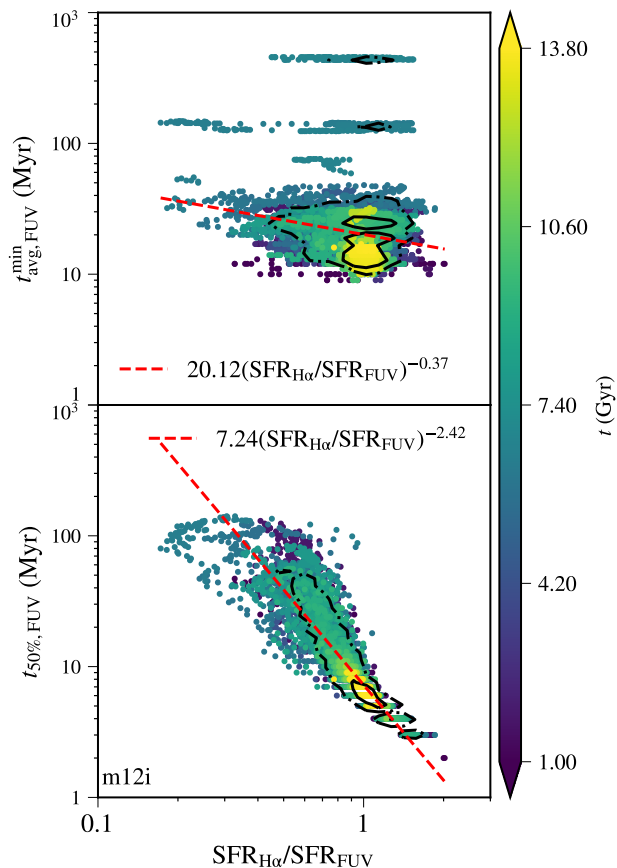
Figure 9. Scatter plots of the best-fitting boxcar-average equivalent time-scale, $t_{\mathrm{avg}}^{\mathrm{min}}$ (top) and the light-weighted median stellar age, $t_{50\%}$, for FUV vs. the instantaneous Hα-to-FUV ratio in m12i. Each dot represents the value at one point of the full SFH, sampled at 1 Myr intervals (in each case, the first 1 Gyr is omitted to avoid edge effects near $t = 0$). 50th and 90th percentile contours are plotted in solid and dot-dashed black respectively. A least-squares best-fitting line is plotted in dashed red, with parameters indicated in each panel. For $t_{\mathrm{avg}}^{\mathrm{min}}$, there is almost no correlation with the SFR ratio because $t_{\mathrm{avg}}^{\mathrm{min}}$ is computed by minimizing over a long time window $T_{\mathrm{w}} = 500$ Myr (see §2.3). As a result, $t_{\mathrm{avg}}^{\mathrm{min}}$ is a poor measure of the recent SFH probed by the instantaneous Hα-to-FUV ratio in bursty phases. On the other hand, like the Hα-to-FUV ratio, $t_{50\%}$ is directly sensitive to the recent SFH and is thus much more tightly anti-correlated with $\mathrm{SFR}_{\mathrm{H}\alpha}/\mathrm{SFR}_{\mathrm{FUV}}$.

SFR, we investigate whether the observed Hα-to-FUV ratio can be used to infer more accurate (i.e. more applicable to the specific time corresponding to the observation) time-scales than the ones listed above that are implied statistically by the FIRE-2 simulated SFHs.

Figure 9 shows a scatter plot of the Hα-to-FUV ratio vs. $t_{\mathrm{avg}}^{\mathrm{min}}$ (top panel) and $t_{50\%}$ (bottom panel), for m12i and cosmic times $1 < t < 13.8$ Gyr spaced by 1 Myr (this includes both times when the SFR is bursty and when it is steady). This figure focuses on FUV time-scales because, owing to their longer values, they are more sensitive to variations in the SFH than Hα. For $t_{\mathrm{avg}}^{\mathrm{min}}$, we see almost no correlation with the SFR ratio. This is because, as we defined it, $t_{\mathrm{avg}}^{\mathrm{min}}$ is computed by minimizing over a long time window $T_{\mathrm{w}} = 500$ Myr. As a result, since the SFR (and consequently the Hα-to-FUV ratio) fluctuates on time scales smaller than T_{w}, during bursty phases $t_{\mathrm{avg}}^{\mathrm{min}}$ is a poor measure of the very recent (or "local") SFH, which is the portion of the SFH probed by the instantaneous Hα-to-FUV

ratio. Thus, within a single window while $t_{\mathrm{avg}}^{\mathrm{min}}$ remains effectively constant the Hα-to-FUV ratio takes many values (both less than and larger than unity) tracing the horizontal lines observed in the top panel of Figure 9, and washing out any correlation between the two.

On the other hand, like the Hα-to-FUV ratio, $t_{50\%}$ is directly sensitive to the SFH at times immediately preceding the time of observation. This results in a much tighter anti-correlation between $t_{50\%}$ and the Hα-to-FUV ratio, visible in the bottom panel of the figure. The slope of relationship is negative because a smaller Hα-to-FUV ratio implies that (on average) the SFR has decreased from the earlier times probed by FUV light to the more recent times probed by Hα light. This implies that the stellar age of the stars below which 50% of the observed FUV luminosity was produced, i.e. $t_{50\%,\mathrm{FUV}}$, is larger (i.e. formed during a recent burst of star formation). Quantitatively, the best-fitting the slope of the power-law relation plotted in the bottom panel of the figure is -2.42 for m12i, though it can vary with galaxy mass and redshift as the statistics of SFR variations evolve. In future work, it would be interesting to more systematically quantify the time-scales probed by SFR indicators as a function of the observed Hα-to-FUV ratio.

4.3 Caveats and possible extensions

In this work, we have neglected attenuation of UV light by dust (e.g., Calzetti et al. 2000; Reddy et al. 2016). Attenuation by dust is in general critical to model to obtain correctly normalized SFR measurements. Since attenuation by dust depends on wavelength, it can also affect the ratio of different SFR indicators, such as the Hα-to-FUV ratio discussed above. However, since we focus on the *time-scales* probed by different indicators, constant dust attenuation would have no effect on our main results.

Dust could in principle modify the time-scales probed by an SFR indicator if the attenuation that it produces is time-dependent and correlated with the light sources (Koyama et al. 2019; Salim & Narayanan 2020). For example, if dust initially obscures star-forming regions but is cleared by stellar feedback after some time, this could modify the effective response function of the indicator. Properly modeling this kind of effect would require accounting for the exact spatial distribution and time-dependence of both the dust and light sources in galaxies, along with a detailed treatment of radiative transfer. Although this is beyond the scope of this work, zoom-in simulations such as the FIRE-2 simulations analyzed in this paper could be combined with existing dust radiative transfer codes (e.g., Jonsson 2006; Camps & Baes 2015; Narayanan et al. 2020) to carry out such a study. This would also make it possible to study SFR indicators resulting from the processing of direct stellar radiation by dust, such as indicators based on IR radiation.

Other possible extensions of this work would be to include the effects of stochastic sampling of the IMF (e.g., da Silva et al. 2014), which could have interesting effects, especially in dwarf galaxies, as well as the effects of an IMF that potentially varies with environment (e.g., van Dokkum & Conroy 2010).

5 CONCLUSIONS

In this paper we quantify the time-scales probed by the FUV and Hα indicators commonly used to measure star formation rates by using star formation histories from FIRE-2 cosmological zoom-in simulations (Hopkins et al. 2018). A key goal of our study is to investigate the effects of realistic SFHs, including secular trends as well as short-term variability ("burstiness"), on the time-scales

probed by standard indicators calibrated to constant SFHs (e.g., Kennicutt & Evans 2012). The SFHs for Milky Way-mass galaxies in the FIRE simulations exhibit a transition from a highly time-variable, or bursty, phase at early times to a time-steady phase at late times. Moreover, dwarf galaxies are bursty at all epochs (Figure 3). Our analysis is on based mock, unattenuated FUV and Hα light curves produced by combining SFHs from FIRE-2 simulations with the BPASS stellar population synthesis model, which includes the effects of binary stars (Eldridge et al. 2017).

We define $t_{\mathrm{avg}}^{\mathrm{min}}$, the best-fitting boxcar-average equivalent time-scale, which is a statistical measure computed in 500 Myr-wide moving windows that cover representative samples of short-time-scale SFR fluctuations (see §2.3). We find that $t_{\mathrm{avg}}^{\mathrm{min}} \sim 5$ Myr for Hα, independent of whether the SFH is bursty or time-steady. On the other hand, $t_{\mathrm{avg}}^{\mathrm{min}}$ fluctuates more during the bursty phase of star formation, from $t_{\mathrm{avg}}^{\mathrm{min}} \sim 10$ Myr to > 100 Myr in cases following particularly extreme bursts of star formation. However, when the SFR becomes time-steady, the FUV $t_{\mathrm{avg}}^{\mathrm{min}}$ approaches ~ 10 Myr (Figure 5). These best-fitting boxcar-average equivalent time-scales are notable because theoretical models often assume that FUV and Hα observations probe SFRs boxcar-averaged over the much longer time-scales of 100 Myr and 10 Myr, respectively (e.g., Orr et al. 2018; Hani et al. 2020). This difference arises because, for example, while stellar populations emit significant FUV for ages exceeding 100 Myr, the integrated UV emission is strongly weighted toward younger, massive stars.

In order to further characterize the distribution of stellar ages contributing to each SFR indicator, we also define $t_{50\%}$ as the light-weighted median stellar age, and analogous quantities for different age percentiles. Unlike $t_{\mathrm{avg}}^{\mathrm{min}}$, $t_{50\%}$ is a local measure of the recent SFH, in the sense that it is computed directly based on the SFH immediately preceding the time of interest (or observation) rather than being a statistical best fit over a large sampling window. We focused our analysis of the stellar age distribution on FUV (Figure 8), which probes a wider age range. For FUV, $t_{50\%}$ fluctuates strongly, from ~ 5 Myr to ~ 50 Myr in the bursty phase for the example shown in the figure. As expected from previous studies, the asymptotic value of $t_{90\%} \sim 100$ Myr is consistent with the time-scale sometimes associated with FUV, defined such that FUV reach 90% of its asymptotic luminosity for a constant SFR. The distribution and time evolution of $t_{x\%}$ values in general depend on the details of the SFH. However, we find that for all simulations that achieve time-steady SFRs at late-times, the $t_{x\%}$ that best matches the late-time $t_{\mathrm{avg}}^{\mathrm{min}}$ is $t_{65\%}$.

We also investigated how the observed Hα-to-FUV ratio can tell us more about the time-scale probed by FUV light. Since Hα and FUV are sensitive to light from stars of different ages, the observed ratio is sensitive to the shape of the recent SFH. In turn, the shape of the recent SFH affects $t_{50\%,\mathrm{FUV}}$. Indeed, the simulations predict a strong anti-correlation between $t_{50\%,\mathrm{FUV}}$ and $\mathrm{SFR}_{\mathrm{H}\alpha}/\mathrm{SFR}_{\mathrm{FUV}}$ (Figure 9). This anti-correlation arises because, in periods following a burst of star formation, the FUV luminosity is dominated by older stars formed during the burst (corresponding to large $t_{50\%,\mathrm{FUV}}$) while the Hα luminosity is dominated by younger stars. Thus, following a burst after which the true SFR decays $\mathrm{SFR}_{\mathrm{H}\alpha}/\mathrm{SFR}_{\mathrm{FUV}}$ decreases to <1. More generally, our results support the use of the Hα-to-FUV ratio as an observational probe of SFR variability (e.g., Weisz et al. 2012).

Finally, we note that there are several avenues for extending the present study, which could lead to further important insights. These include the effects of dust attenuation and reprocessing of stellar light into IR indicators, stochastic sampling and possible environmental variations of the IMF, as well as the use of more detailed panchromatic data.

DATA AVAILABILITY

The data supporting the plots within this article are available on reasonable request to the corresponding author. A public version of the GIZMO code is available at http://www.tapir.caltech.edu/~phopkins/Site/GIZMO.html. Additional data including simulation snapshots, initial conditions, and derived data products are available at http://fire.northwestern.edu/data/.
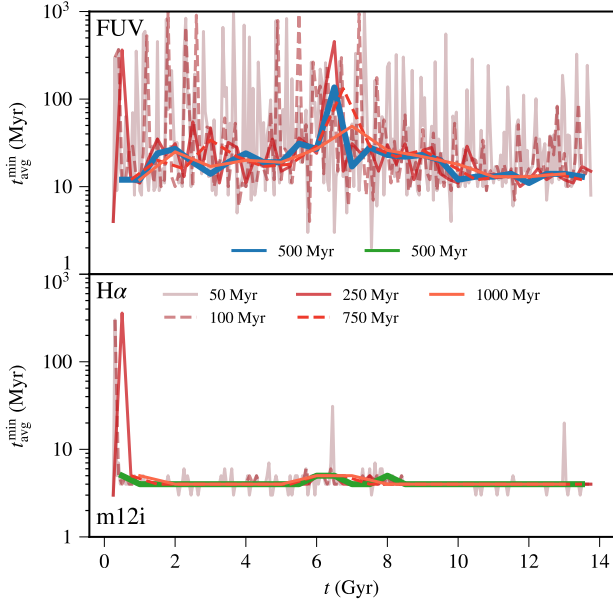
Figure A1. History of $t_{\mathrm{avg}}^{\min}$ over cosmic time for FUV (top) and Hα (bottom) in non-overlapping windows for different choices of window width T_{w} (indicated by color) in m12i. For sufficiently large T_{w} ($\gtrsim 250$ Myr for FUV and $\gtrsim 50$ Myr for Hα) $t_{\mathrm{avg}}^{\min}$ is relatively insensitive to the choice of T_{w}.

APPENDIX A: DEPENDENCE OF OUR RESULTS ON WIDTH T_{W} OF THE TIME WINDOW

In §2.3 we define $t_{\mathrm{avg}}^{\min}$, the best-fitting boxcar-average equivalent time-scale for ensembles of points in SFHs grouped in moving windows of fiducial width $T_{\mathrm{w}} = 500$ Myr. In Figure A1 we show that the choice of T_{w}, for sufficiently large T_{w}, does not affect the inferred average value of $t_{\mathrm{avg}}^{\min}$. For Hα (bottom panel), $t_{\mathrm{avg}}^{\min}$ is largely insensitive to the window size so long as it is larger than $T_{\mathrm{w}} = 50$ Myr (save for the first 1 Gyr, which is affected by edge effects near $t = 0$). On the other hand, FUV (top panel) shows stronger variations for $T_{\mathrm{w}} < 250$ Myr, but above this value $t_{\mathrm{avg}}^{\min}$ is well converged.

REFERENCES

Agertz O., Kravtsov A. V., 2015, ApJ, 804, 18
Anglés-Alcázar D., Faucher-Giguère C.-A., Kereš D., Hopkins P. F., Quataert E., Murray N., 2017, MNRAS, 470, 4698
Brinchmann J., Charlot S., White S. D. M., Tremonti C., Kauffmann G., Heckman T., Brinkmann J., 2004, MNRAS, 351, 1151
Bruzual G., Charlot S., 2003, MNRAS, 344, 1000
Bryan G. L., Norman M. L., 1998, ApJ, 495, 80
Buat V., et al., 2012, Proceedings of the International Astronomical Union, 10, 495âĂŞ527
Calzetti D., 2013, Star Formation Rate Indicators. p. 419
Calzetti D., Armus L., Bohlin R. C., Kinney A. L., Koornneef J., Storchi-Bergmann T., 2000, ApJ, 533, 682
Calzetti D., et al., 2007, ApJ, 666, 870
Camps P., Baes M., 2015, Astronomy and Computing, 9, 20
Conroy C., Gunn J. E., White M., 2009, ApJ, 699, 486
Domínguez A., Siana B., Brooks A. M., Christensen C. R., Bruzual G., Stark D. P., Alavi A., 2015, MNRAS, 451, 839
Elbaz D., et al., 2007, A&A, 468, 33
Elbaz D., et al., 2018, A&A, 616, A110
Eldridge J. J., Stanway E. R., Xiao L., McClelland L. A. S., Taylor G., Ng

M., Greis S. M. L., Bray J. C., 2017, Publ. Astron. Soc. Australia, 34, e058
Emami N., Siana B., Weisz D. R., Johnson B. D., Ma X., El-Badry K., 2019, ApJ, 881, 71
Faucher-Giguère C.-A., 2018, MNRAS, 473, 3717
Faucher-Giguère C.-A., Hopkins P. F., Kereš D., Muratov A. L., Quataert E., Murray N., 2015, MNRAS, 449, 987
Faucher-Giguère C.-A., Feldmann R., Quataert E., Kereš D., Hopkins P. F., Murray N., 2016, MNRAS, 461, L32
Ferland G. J., Korista K. T., Verner D. A., Ferguson J. W., Kingdon J. B., Verner E. M., 1998, PASP, 110, 761
Fitts A., et al., 2018, MNRAS, 479, 319
Forrest B., et al., 2017, ApJ, 838, L12
Fumagalli M., da Silva R. L., Krumholz M. R., 2011, ApJ, 741, L26
Garrison-Kimmel S., et al., 2017, MNRAS, 471, 1709
Garrison-Kimmel S., et al., 2019, MNRAS, 487, 1380
Gill S. P. D., Knebe A., Gibson B. K., 2004, MNRAS, 351, 399
Governato F., et al., 2012, MNRAS, 422, 1231
Guo Y., et al., 2016, ApJ, 833, 37
Gurvich A. B., et al., 2020, arXiv e-prints, p. arXiv:2005.12916
Hafen Z., et al., 2017, MNRAS, 469, 2292
Hani M. H., Hayward C. C., Orr M. E., Ellison S. L., Torrey P., Murray N., Wetzel A., Faucher-Giguère C.-A., 2020, MNRAS, 493, L87
Hao C.-N., Kennicutt R. C., Johnson B. D., Calzetti D., Dale D. A., Moustakas J., 2011, ApJ, 741, 124
Hayward C. C., et al., 2014, MNRAS, 445, 1598
Hirtenstein J., et al., 2019, ApJ, 880, 54
Hopkins P. F., 2015, MNRAS, 450, 53
Hopkins P. F., Narayanan D., Murray N., 2013, MNRAS, 432, 2647
Hopkins P. F., Kereš D., Oñorbe J., Faucher-Giguère C.-A., Quataert E., Murray N., Bullock J. S., 2014, MNRAS, 445, 581
Hopkins P. F., et al., 2018, MNRAS, 480, 800
Iyer K. G., Gawiser E., Faber S. M., Ferguson H. C., Kartaltepe J., Koekemoer A. M., Pacifici C., Somerville R. S., 2019, ApJ, 879, 116
Jonsson P., 2006, MNRAS, 372, 2
Kennicutt Jr. R. C., Evans N. J., 2012, Annual Review of Astronomy and Astrophysics, 50, 531
Knollmann S. R., Knebe A., 2009, ApJ, 182, 608
Koyama Y., et al., 2015, MNRAS, 453, 879
Koyama Y., Shimakawa R., Yamamura I., Kodama T., Hayashi M., 2019, PASJ, 71, 8
Kroupa P., Tout C. A., Gilmore G., 1993, MNRAS, 262, 545
Leitherer C., et al., 1999, ApJ, 123, 3
Ma X., Hopkins P. F., Faucher-Giguère C.-A., Zolman N., Muratov A. L., Kereš D., Quataert E., 2016a, MNRAS, 456, 2140
Ma X., Hopkins P. F., Kasen D., Quataert E., Faucher-Giguère C.-A., Kereš D., Murray N., Strom A., 2016b, MNRAS, 459, 3614
Ma X., Hopkins P. F., Feldmann R., Torrey P., Faucher-Giguère C.-A., Kereš D., 2017, MNRAS, 466, 4780
Matthee J., Schaye J., 2019, MNRAS, 484, 915
Muratov A. L., Kereš D., Faucher-Giguère C.-A., Hopkins P. F., Quataert E., Murray N., 2015, MNRAS, 454, 2691
Murphy E. J., et al., 2011, ApJ, 737, 67
Narayanan D., et al., 2020, arXiv e-prints, p. arXiv:2006.10757
Noeske K. G., et al., 2007, ApJ, 660, L43
Orr M. E., et al., 2017, ApJ, 849, L2
Orr M. E., et al., 2018, MNRAS, 478, 3653
Pelliccia D., et al., 2020, ApJ, 896, L26
Reddy N. A., Steidel C. C., Pettini M., Bogosavljević M., 2016, ApJ, 828, 107
Salim S., Narayanan D., 2020, arXiv e-prints, p. arXiv:2001.03181
Salim S., Lee J. C., Ly C., Brinchmann J., Davé R., Dickinson M., Salzer J. J., Charlot S., 2014, ApJ, 797, 126
Schreiber C., et al., 2015, A&A, 575, A74
Shivaei I., et al., 2015, ApJ, 815, 98
Smit R., Bouwens R. J., Labbé I., Franx M., Wilkins S. M., Oesch P. A., 2016, ApJ, 833, 254

Sparre M., Hayward C. C., Feldmann R., Faucher-Giguère C.-A., Muratov A. L., Kereš D., Hopkins P. F., 2017, MNRAS, 466, 88

Stern J., et al., 2020, arXiv e-prints, p. arXiv:2006.13976

Teyssier R., Pontzen A., Dubois Y., Read J. I., 2013, MNRAS, 429, 3068

Weisz D. R., et al., 2012, ApJ, 744, 44

Whitaker K. E., van Dokkum P. G., Brammer G., Franx M., 2012, ApJ, 754, L29

Willett K. W., et al., 2015, MNRAS, 449, 820

da Silva R. L., Fumagalli M., Krumholz M., 2012, ApJ, 745, 145

da Silva R. L., Fumagalli M., Krumholz M. R., 2014, MNRAS, 444, 3275

van Dokkum P. G., Conroy C., 2010, Nature, 468, 940

van der Wel A., et al., 2011, ApJ, 742, 111

This paper has been typeset from a TEX/LATEX file prepared by the author.